Additive Manufacturing 36 (2020) 101442

Contents lists available at ScienceDirect

Additive Manufacturing

journal homepage: www.elsevier.com/locate/addma

Effects of post-processing route on fatigue performance of laser powder bed fusion Inconel 718

Dennise Tanoko Ardi[a,*], Lim Guowei[a], Niroj Maharjan[a], Bisma Mutiargo[a], Seng Hwee Leng[b], Raghavan Srinivasan[a]

[a] Advanced Remanufacturing and Technology Centre, A*STAR (Agency for Science, Technology and Research), 3 Cleantech Loop #01-01, 417392, Singapore
[b] Institute of Materials Research and Engineering, A*STAR (Agency for Science, Technology and Research), 2 Fusionopolis Way, Innovis, 138634, Singapore

ARTICLE INFO

Keywords:
Additive manufacturing
Laser powder bed fusion
Shot peening
Hot isostatic pressing
Inconel 718

ABSTRACT

Fatigue performance of Inconel 718 (IN718) parts built using laser powder bed fusion (L-PBF) is often poorer than that of the cast and wrought alloy parts. This is because of detrimental effects arising from the microstructures such as brittle phases and anisotropy as well as porosities. To improve fatigue performance of L-PBF IN718, two types of post processes namely hot isostatic pressing (HIP) (performed at 980 °C, 100 MPa and 4 h) and shot peening (performed at 0.45 mmA intensity and 200 % coverage) were employed individually as well as sequentially on different specimens in addition to a standard processing route consisting of L-PBF build followed by solution annealing and double aging heat treatment. Porosities were considerably reduced by HIP-ing (from 0.39 % to 0.08 % porosity volume ratio) but this did not translate to improvements in fatigue performance. This can be attributed to the presence of inclusions and yield strength reduction resulting from γ" solutionisation. High compressive residual stresses of close to 1 GPa were recorded following shot peening regardless of whether HIP-ing was carried out prior to the shot peening. Improvement in fatigue lives particularly at high stress levels was observed on shot peened specimens without HIP-ing (H + SP) which can be explained by the compressive residual stresses that delay the onset of fatigue crack initiation. Shot peening applied on the HIP-ed specimens (H + HIP + SP) however, resulted in fatigue performance deterioration. This is related to the harmful tensile stresses that must exist alongside the compressive residual stresses in a shot peened surface, as evident from the location of the sub-surface crack initiations near the residual stress transition region approximately 300 μm from the free surface. In this case, detrimental effects arising from tensile stresses appear to have outweighed the benefits from compressive stresses on fatigue performance.

1. Introduction

Laser powder bed fusion (L-PBF) parts are known to contain defects and pores which are particularly detrimental to fatigue [1]. Porosities are introduced within the built parts through shrinkage [2], existing pores in the powder [3,4], gas entrapments [5,6], lack of fusion [2] and keyhole formation [7,8]. As the energy density being utilised in L-PBF process is increased, porosities formation with keyhole geometry have also been observed [7,8]. At high energy densities, remarkable change in meltpool geometry from bowl shape (low energy densities) to keyhole shape was observed due to the change in heat transfer mode from primarily conduction and convection to keyhole mode [8]. Gas bubbles may form at keyhole meltpool from vapourisation of low melting point constituents within the alloy [7]. The recoil pressure from the vapourisation lead to melt pool collapsing upon itself entrapping the metal vapour resulting in the keyhole porosity [10,11]. Keyhole porosities have been largely avoided through optimisation of the energy density as demonstrated in recent studies on L-PBF Inconel 718 (IN718) [2,5,12]. Shrinkage pores are usually found in between deposited layer when thermal contraction due to solidification is being hindered by the previously solidified layer underneath. Shrinkage pores have been observed particularly in electron powder bed fusion processes (E-PBF) IN718 but not in the L-PBF [2].

Post-processing techniques can be employed to reduce the porosities in L-PBF parts. Hot isostatic pressing (HIP) has been successfully implemented to reduce porosities in L-PBF IN718 through the application of high ambient pressure at elevated temperatures [12–14]. The process was found to be effective in reducing the size and number of pores. However, it is not expected to completely eliminate them even when the pressure is increased beyond 100 MPa [13]. Gas pores for instance,

* Corresponding author.
E-mail address: denniseta@artc.a-star.edu.sg (D.T. Ardi).

https://doi.org/10.1016/j.addma.2020.101442
Received 11 April 2020; Received in revised form 29 June 2020; Accepted 5 July 2020
Available online 08 July 2020

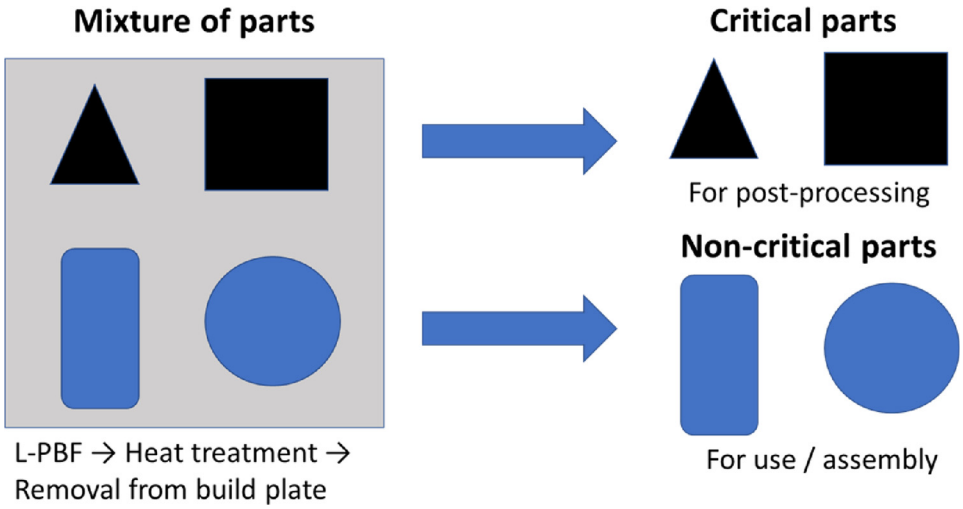

Fig. 1. A schematic of L-PBF production where critical and non-critical parts are built within a single platform. Critical parts are subject to subsequent post-processing and non-critical parts are ready for its application.

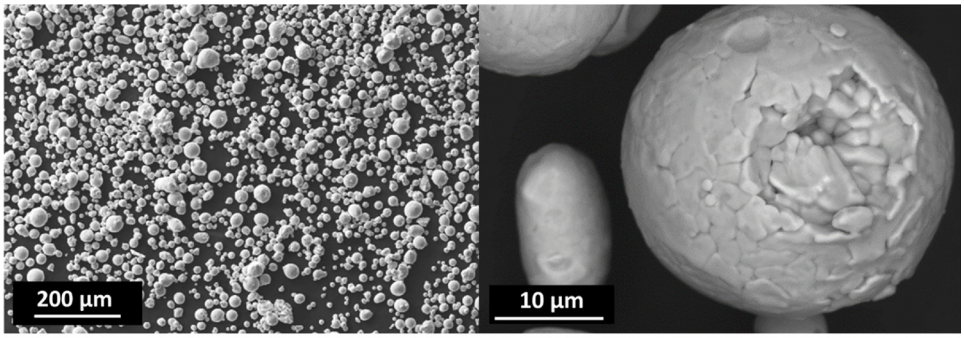

Fig. 2. Secondary electron micrographs of the gas-atomised IN718 powder: (a) at low magnification showing the range of powder size and circularity of the powder and (b) at high magnification highlighting its imperfection.

Table 1
Chemical composition (excluding trace elements) of gas atomized IN718 powder supplied by EOS-GmbH.

Ni	Cr	Mo	Nb	Ti	Al	Fe
53.95	18.28	3.04	5.12	1.02	0.50	Balance

cannot be eliminated as argon does not diffuse readily into the metal [9,13] owing to its large atomic diameter. The location of pores within a built part is also crucial in controlling the fatigue performance. Near-surface pores are particularly harmful as they tend to initiate fatigue cracks. In L-PBF IN718 as-built parts, pores have been found to be clustered in the near-surface [15] as well as around the boundary between core and shell regions where different scanning strategies are employed [13,16].

Surface engineering techniques such as shot peening and deep cold rolling are known to improve fatigue performance of metallic alloys by introducing compressive residual stresses in the near-surface as well as improving the surface finish in some cases (e.g. deep cold rolling). Studies demonstrating their effectiveness for AM alloys' fatigue performance improvements have been carried out using ultrasonic shot peening/impact treatment [17] deep cold rolling [18], shot peening [17,19,20] and laser shock peening [21–23]. Some of these techniques have even been implemented to improve the microstructure and residual stresses throughout the bulk of the material. This was achieved by employing the surface engineering process at intermediate stages of the build (i.e. inter-layer processing) [23–25].

The application of both HIP-ing and shot peening may result in a synergistic effect in enhancing the fatigue performance of L-PBF IN718 parts [26]. A number of investigations of the AM IN718 fatigue performance have also been reported [16,27–30] considering different processing routes. In this study, we are focusing on the investigation of surface integrity as well as fatigue performance exhibited by L-PBF IN718 specimens subjected to *additional* post-processing routes consisting of HIP-ing and/or shot peening following a chain of an established process for industrialisation of L-PBF IN718. This is based on the premise that in a production of multiple parts within a single build, only critical parts will be subjected to additional post-processing as illustrated in Fig. 1. Experimental studies were carried out using L-PBF parts produced using the established process chain as the baseline, limiting the variations in mechanical properties only to those arising from post-processing methods.

2. Experimental details

2.1. Materials and processing parameters

Gas atomized IN718 powder, supplied by EOS-GmbH with an average diameter of approximately 30 µm with sizes in the range of 19.85 (D_{10}) to 52.12 µm to (D_{90}) was used as the powder feedstock (see Fig. 2). Chemical composition of the powder (excluding trace elements) is listed in Table 1.

L-PBF process was carried out using EOSINT® M290 with the laser power fixed at 285 W at a scanning speed of 960 mm/s. Near-net shape

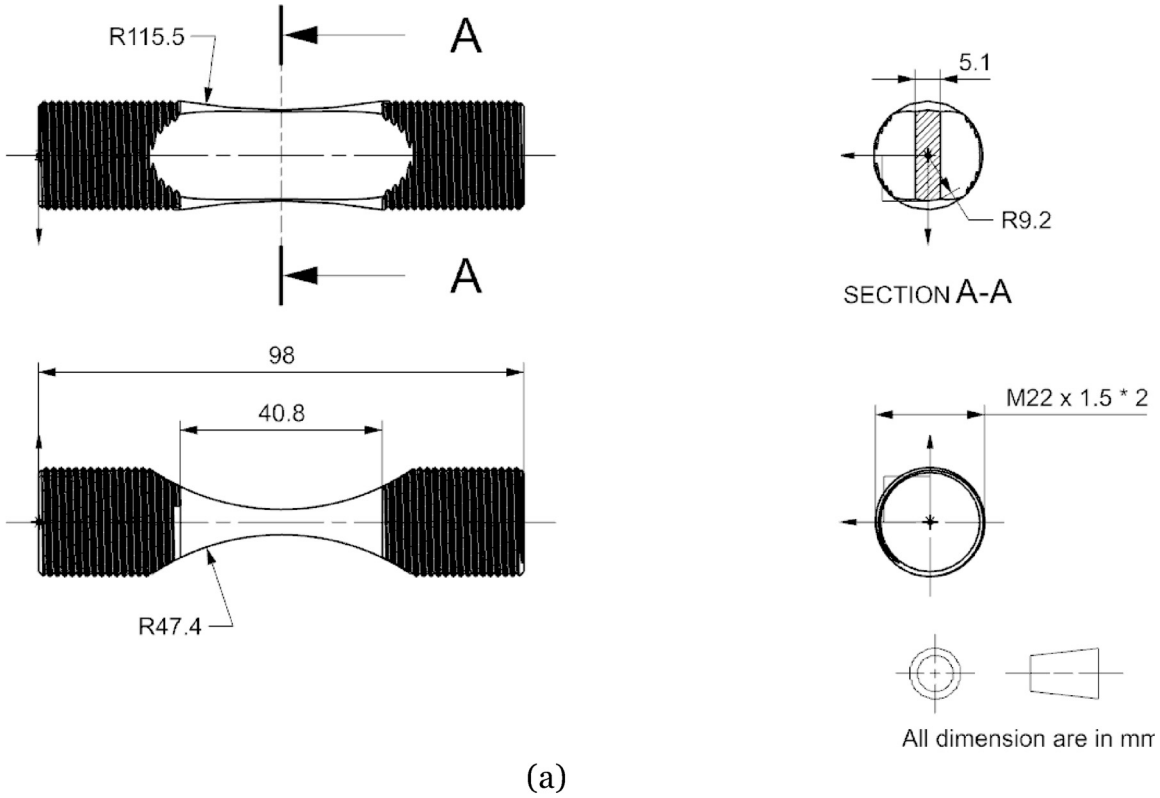

Fig. 3. (a) technical drawing of the fatigue specimen and (b) photograph of the near net-shape L-PBF fatigue specimens.

Table 2
Specimens condition and details of their preparation route.

No.	Designation	Condition	Details
1	P	As-printed	EOSINT® M290, 40 μm layer thickness, 100 μm beam size, 285 W, 960 mm/s scanning speed, 67° rotation applied at each layer.
2	H	Solution annealed and aged	Solution heat treatment at 980 °C for 1 h, followed by air cool (cooling rate of 100 °C/min approx.) Aging heat treatment at 720 °C for 8 h, furnace cool to 620 °C in 2 h, hold at 620 °C for 8 h, followed by air cool (cooling rate of 100 °C/min approx.)
3	H + HIP	Solution annealed, aged and HIP-ed	H +980 °C for 4 h at 100 MPa followed by rapid cooling at approx. 42 °C/min.
4	H + SP	Solution annealed, aged and shot peened	H + shot peening at 0.45 mmA, 200 % coverage and ASH230 media
5	H + HIP + SP	Solution annealed, aged, HIP-ed and shot peened	Same HIP and SP parameters were used sequentially

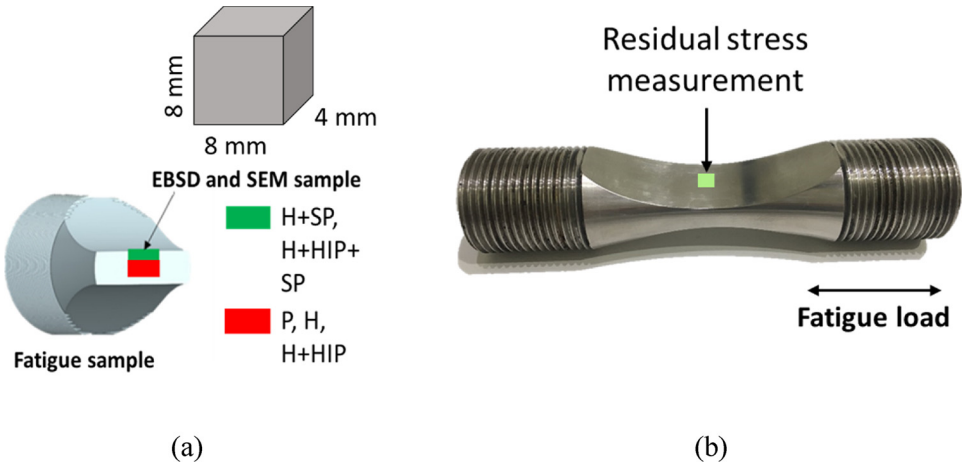

Fig. 4. (a) location of samples extracted for microstructural studies using EBSD and SEM and (b) location of residual stress measurements on the fatigue specimens.

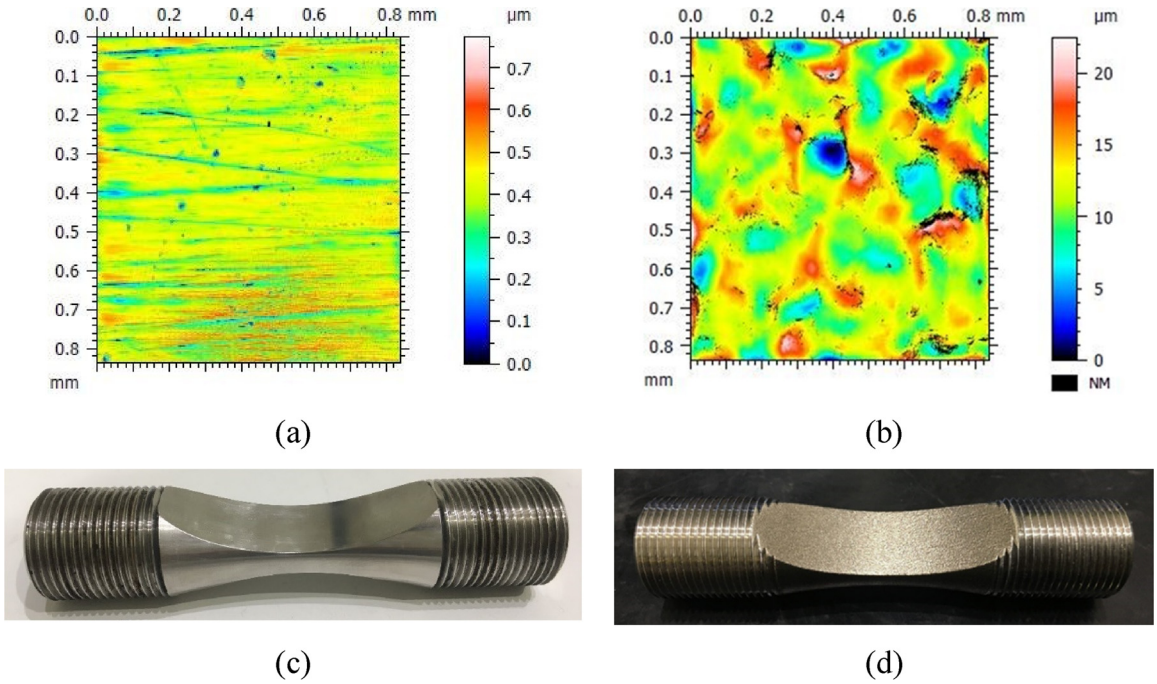

Fig. 5. Representative surface topography maps obtained from: (a) polished surfaces (H and H + HIP) and (b) shot peened surfaces (H + SP and H + HIP + SP). Photographs of the fatigue specimens obtained from: (c) polished and (d) shot peened surfaces.

coupons were built using 100 µm beam spot resulting in each layer measuring approximately 40 µm thick with hatch spacing of 80 µm. The employed L-PBF parameters translate to an energy density of 92.8 J/mm^3, computed using equation below [8]. Where E is energy density, P is laser power, v is scanning speed, h is hatch spacing and t is layer thickness.

$$E = \frac{P}{v \times h \times t}$$

The specimen design and build orientation are shown in Fig. 3. An optimised build strategy where the scanning pattern was rotated by 67° after each layer was employed to reduce anisotropy.

After the build cycle is completed, specimens were separated from the build platform using electric discharge machining and subsequently machined as well as surface finished to produce the fatigue specimens. Four distinct post-processing routes were applied to the coupons as summarised in Table 2.

2.2. Characterisation

Surface topography of the fatigue specimens after polishing and shot peening operations were characterised using Taylor Hobson CCI white light interferometer fitted with a 20x objective lens and with an approximate field of view of 830 by 830 µm. Raw data was processed using a Robust Gaussian filter with cut-off length of 800 µm. Filtering procedure and computation of topography parameters were performed using Talymap Gold software which is compliant to ISO25178 and ASME B46.1.

Rectangular specimens for microstructural characterisation were extracted from fatigue specimens using electric discharge machining, see Fig. 4a. These specimens were mounted in an epoxy resin before being ground and polished using emery paper with progressively finer grit size and diamond suspensions. Microstructural imaging was carried out using a field emission scanning electron microscope (FESEM), JEOL JSM7600 F equipped with Oxford Instruments NordlysNano EBSD detector.

Electro-chemical polishing was applied to the specimens used for

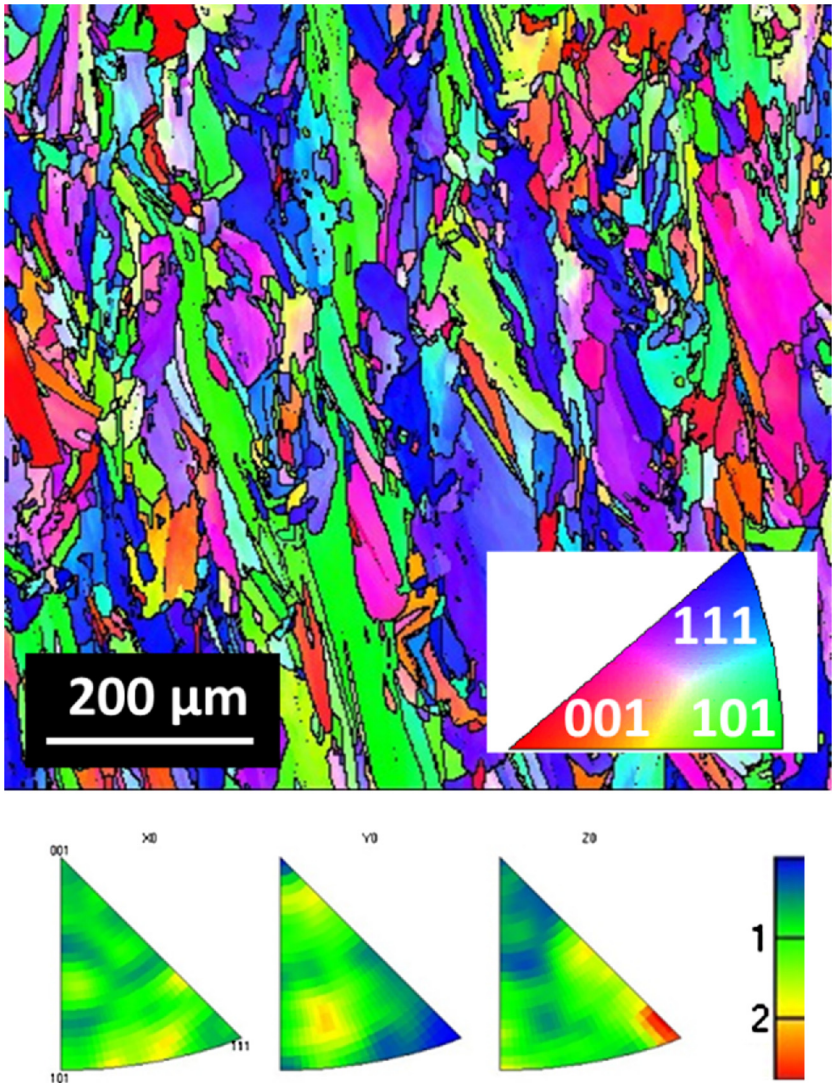

Fig. 6. Inverse pole figures obtained from specimen P showing weak overall texture.

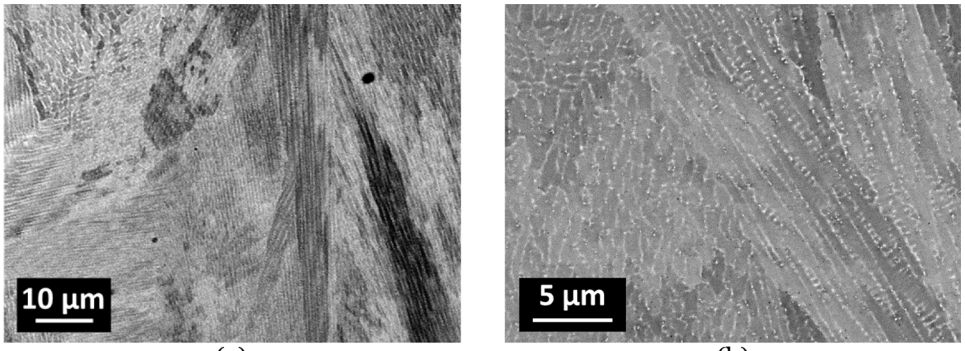

(a) (b)

Fig. 7. Scanning electron micrographs obtained from cross-sectioned specimen P showing: (a) variation in the microstructure (dendritic arm spacing) in laser overlapping region stemming from variation in cooling rates and (b) fine Laves phases distributed evenly in the matrix.

electron back-scatter diffraction (EBSD) experiments. Crystallographic orientation mapping was acquired from the near surface region as shown in Fig. 4. Grain size analysis was carried out to determine the average grain diameter from the acquired EBSD map region. The averaged grain diameter was computed from all grains detected, excluding those which are found at the border (i.e. cut-off). FESEM images were used for observation of secondary phases in the alloy.

Porosities of specimens H and H + HIP were characterised at the gauge section (where fatigue failures are expected to occur) using micro X-ray computed tomography (µXCT), Nikon XTH 225 ST. µXCT is a non-destructive method that is widely used for characterisation of sizes, shapes and distribution of pores in three-dimension (3D). Tomographic imaging was completed in reflection mode at 223 kV and 22.3 mA resulting in a beam spot and a voxel size of 6 and 10 µm respectively. A

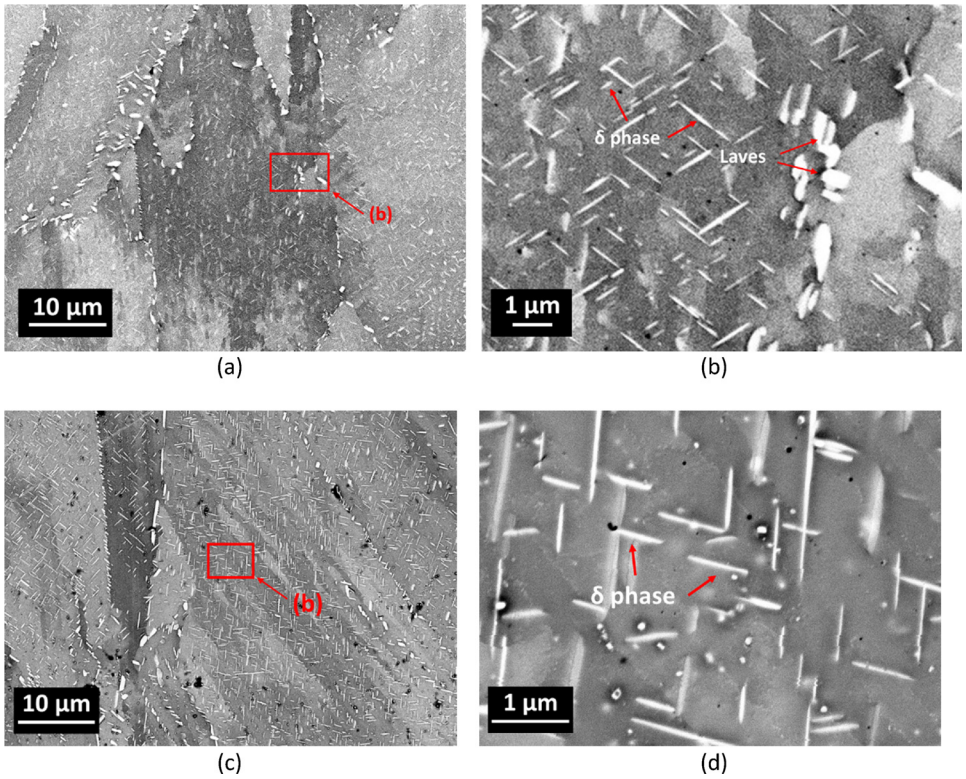

Fig. 8. FESEM micrographs from specimen H (a and b) and H + HIP (c and d) at two different magnification levels. Locations of the high magnification image as indicated in (a and c). Acicular δ were found distributed in the matrix while Laves clustered around the grain boundary.

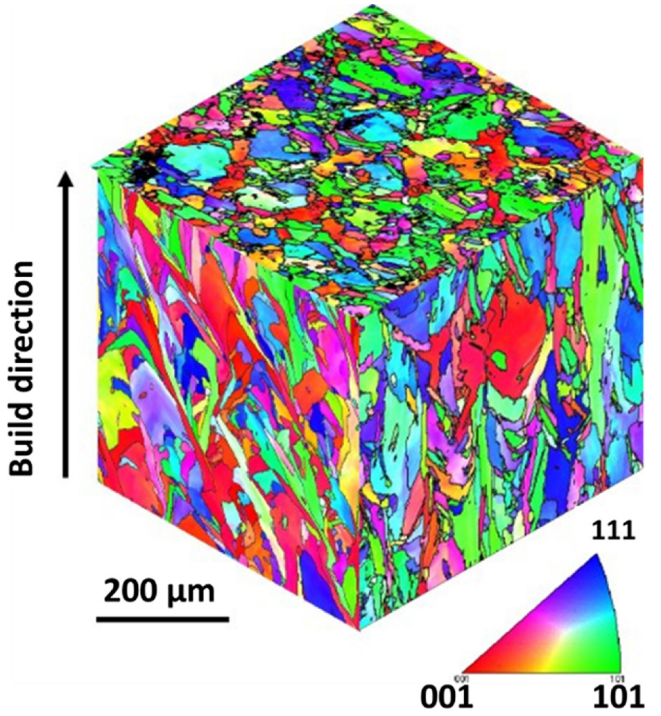

Fig. 9. Inverse pole figure (IPF) colour maps obtained from specimen H at three orthogonal directions with the build direction indicated.

0.25 mm Sn filter was placed between the specimen and the X-ray source to reduce the beam-hardening effect. Prior to image acquisition, a shading correction was also carried out on the detector with 60 images over four energy intervals. In total, 3160 radiography images were captured over 360 degrees of rotation per specimen. These images were employed to reconstruct a 3D model using Nikon CT PRO-3D with automatic beam hardening correction. The surface contour of the 3D model was determined in accordance to ISO-50 and the porosity was then analysed using VGDefX algorithm within the investigated volume of approximately 75 mm^3. A filter was applied to isolate pores with sphericity range of 0.35–1 with a minimum diameter of 40 µm (approximately 4 voxels) to avoid including artefacts from the tomography. Optical microscopy images (50X magnification) were obtained from specimen H to determine the morphology of the porosities.

Vickers hardness micro-indentation experiments were carried out on polished cross-sectioned surface using Innovatest Falcon 510. All measurements were completed using 500gf with a dwell period of 10 s at different locations away from the free surface. Three measurements were completed at each depth when carrying out the hardness vs depth profiling. Nano-indentation experiments were completed using Agilent G200 nanoindentor with a Berkovich indentation tip. Nano-indentation tests were carried out in displacement control for data collection at up to 1000 nm indentation depth. Averaged hardness values collected at indentation depth between 900 and 1000 nm were used for the evaluation. Ten measurements were completed in the bulk material for each of the H and H + HIP conditions.

Residual stress characterisation was carried out using centre-hole drilling (CHD) technique, SINT Technology Restan MTS-3000. CHD is a strain relieving technique which correlates the amount of strain being relieved on the surface with residual stresses at depth increments using algorithm described in ASTM E837-13 for non-uniform stress analysis. TML FRS-2-11-1LT (Type A) strain gauge rosette was affixed to the specimen's surface (location as shown in Fig. 4b) using Z70 cyanacrylate adhesive prior to drilling. Incremental depth drilling was carried out at increasing intervals from 10 µm in the first 100 µm then 25 µm for the next 400 µm and finally 50 µm for the next 700 µm resulting in a total hole depth of 1200 µm for determination of residual stresses at up to 0.975 mm depth. Young's modulus and Poisson ratio of 207.6 GPa and 0.29 respectively were utilised for the computation of residual

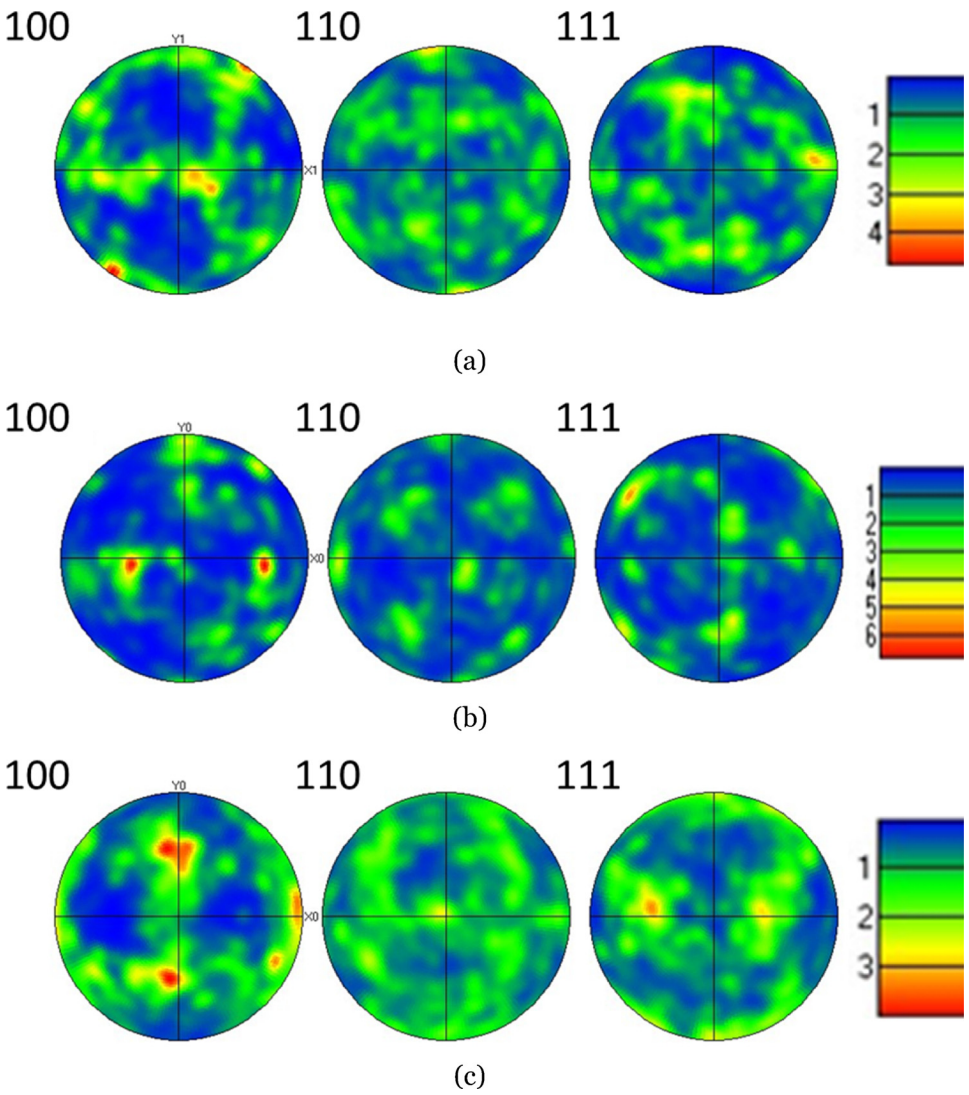

Fig. 10. Pole figures obtained from specimen H with half width and cluster size of 10° and 5° respectively: (a) and (b) were obtained from planes parallel while (c) was taken from the plane perpendicular to the build direction.

stresses with the assumption that changes in these properties after shot peening were negligible.

2.3. Fatigue testing

Uniaxial force-controlled fatigue tests were carried out using an MTS Landmark servo-hydraulic with 250 kN load capacity. All tests were carried out in ambient temperature at a frequency of 20 Hz and an R-ratio of 0.1 (i.e. no compression). Appropriate stress levels were selected to develop a peak stress vs cycle-to-failure (S-N) plot between 10^4 and 10^6 cycles based on typical applications of the alloys.

Cylindrical threaded-end plain (K_t = 1.0) fatigue specimens with continuously varying cross-section (see Fig. 3a) were machined out of the near net-shape AM parts, see Fig. 4b. The cross-section area of the specimen at its gauge section is approximately 92.5 mm2. The fatigue specimen design was selected to allow for application of strain gauge for CHD residual stress characterisation. The specimens were hand-polished to achieve very low surface roughness after machining and prior to shot peening. Fractured surfaces were examined using a scanning electron microscope fitted with secondary electron for imaging.

3. Results and discussions

3.1. Surface topography

Two types of surface topography were characterised following polishing operations (H and H + HIP) and shot peening (H + SP and H + HIP + SP). The averaged roughness (S_a) values increased significantly following shot peening from 0.05 μm to 2.23 μm due to the overlapping dimples introduced through collisions between the specimens' surface and hard shot media (see Fig. 5 for representative topography maps and photographs of the two types of surface topography).

3.2. Microstructure

Typical microstructures of the as-built IN718 specimen were found to exhibit elongated grains aligned with the build direction with some grains spanning across as long as several hundred μm (see Fig. 6). This is consistent with typical materials built using L-PBF [31]. Strong texturing was not observed in the specimen (refer to inverse pole figure (IPF) map in Fig. 6) which is attributed to the optimised build strategy [29,32]. Such rotations prevent the directional growth of columnar dendrite resulting in the observed weak texture [29,33]. The degree of texturing is known to be controlled mainly by the predominant heat

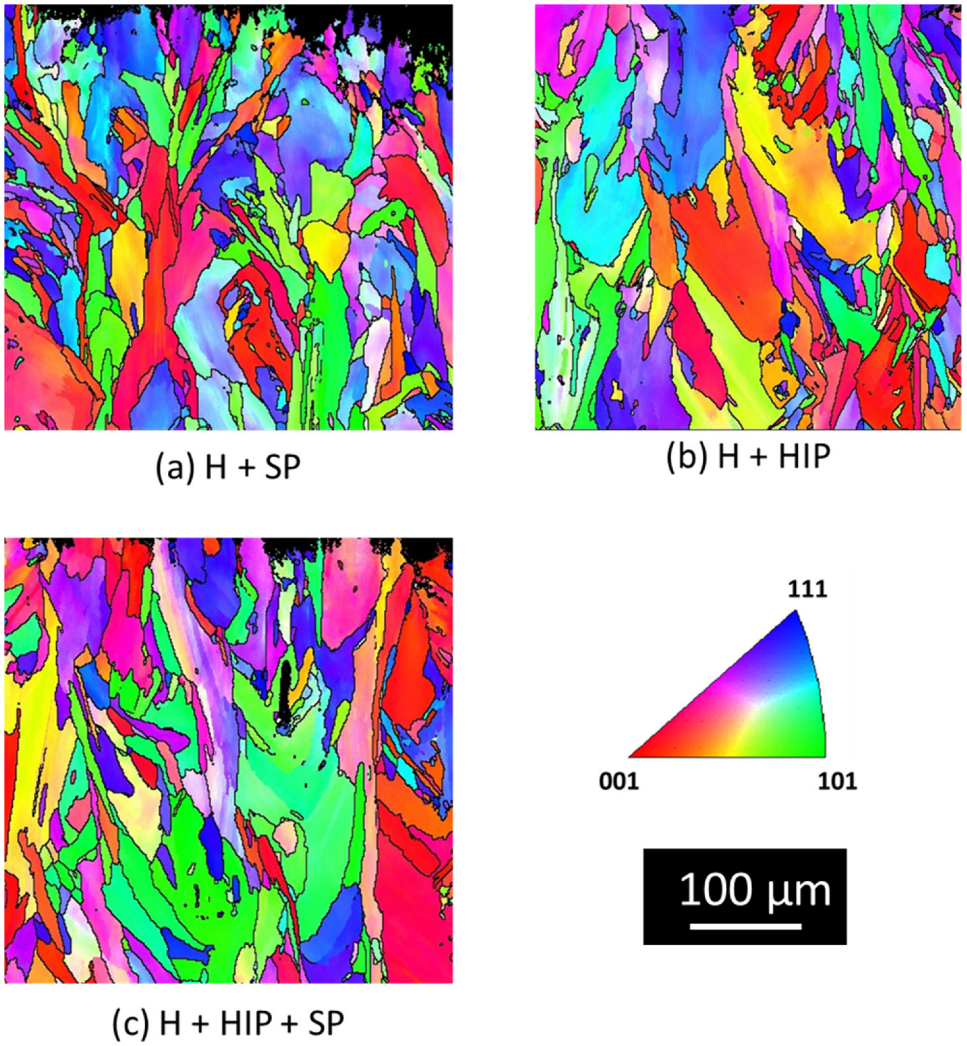

Fig. 11. Inverse pole figure (IPF) colour maps obtained from specimens following post-processing (a) H + SP, (b) H + HIP and (c) H + HIP + SP.

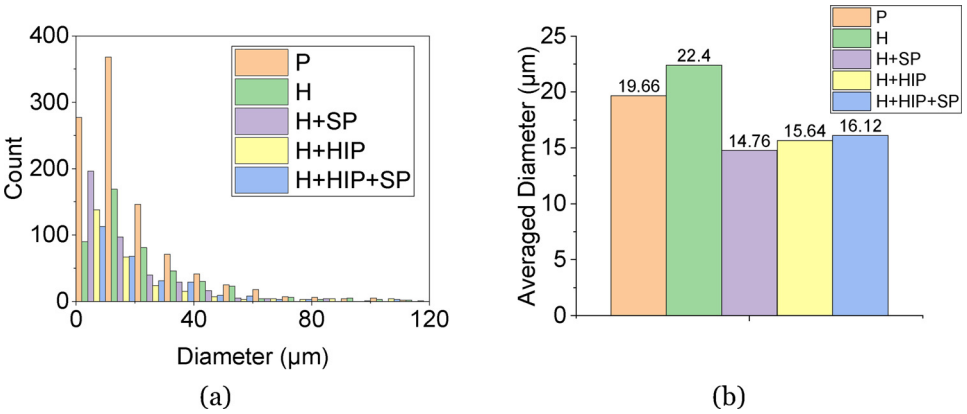

Fig. 12. Grain size statistics obtained from the different specimens: (a) histograms of equivalent diameters distribution and (b) averaged equivalent diameters.

flux direction during the build process [16,34,35].

Laves phases are formed at high temperature due to Nb segregations [3]. The brittle Laves phases were observed in the as-built sample in the interdendritic region with chain-like arrangement (see Fig. 7). While Laves phases can be beneficial for high-cycle fatigue [36], they are generally detrimental to mechanical properties as they act as stress-raisers [37,38]. Furthermore, since Nb is a major constituent of strengthening phases γ' and γ", its segregation also directly impacts the distribution of these strengthening precipitates. Solution annealing heat treatment was therefore performed to dissolve Laves phases and reduce residual anisotropy associated with the printing process.

Homogenisation heat treatment applied to as-print IN718 was found to encourage dissolution of Laves precipitates into the matrix and precipitate needle-like δ phases consistent with findings in the literature [39–41]. Due to a lower temperature (980 °C) used for solution annealing [3], residual Laves phases could still be observed near the grain

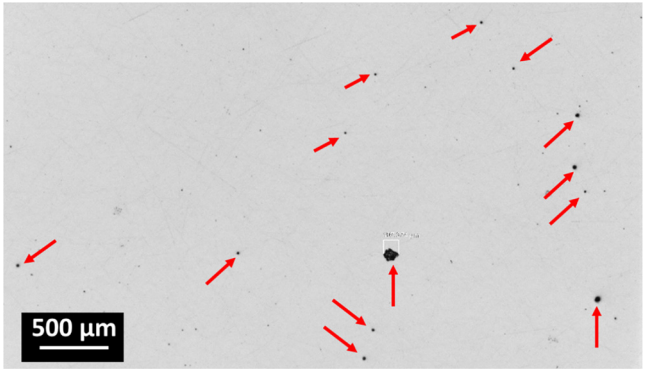

Fig. 13. Optical microscope image obtained from specimen H showing gas pores being distributed randomly across the cross-section. The largest pore shown in this image has a diameter of 107 µm. Large pores detected are indicated by red arrows.

boundary as they were not dissolved during the annealing treatment (see Fig. 8a and b). Double aging heat treatment according to AMS5663 was subsequently applied to the homogenised specimens to encourage formation of γ" strengthening precipitates. Similar microstructures comprising of finely distributed acicular δ phases and Laves were exhibited by the specimen after HIP-ing (see Fig. 8c and d)

Fig. 9 shows EBSD inverse pole figure (IPF) colour maps obtained from the three orthogonal planes after solution annealing and double ageing heat treatment. The maps reveal elongated (columnar) grains along the build direction with fairly large grains interspersed with fine grains. This is due to the L-PBF process where rapid heat dissipation along the build direction is expected to occur. Equiaxial grains were observed perpendicular to the build direction. The average grain size along and perpendicular to the build direction were ~24 µm and ~17µm respectively. The overall texture is random (i.e. no clear preferred orientation) as evident from the pole figures shown in Fig. 10.

The random crystallographic orientation structure does not appear to have been altered by HIP-ing and shot peening as shown in the IPF maps (see Fig. 11). Grain refinement can be observed following the different post-processing (see Fig. 11). A histogram of equivalent diameter obtained from individual grain was plotted for each condition to compare the distribution of grain sizes in specimens of different conditions (see Fig. 12a). The histogram as well as the IPF maps reveal a large number of small grains interspersed between the large grains. HIP-ing reduced the averaged grain size through the introduction of recrystallized grains. The reduction in the averaged grain size in shot peened specimens on the other hand appear to have been driven by the reduction in the width of the large columnar grains through plastic deformation. The extent of grain refinement was observed to be similar for the different post-processing routes.

3.3. Porosity evaluation

Optical images obtained from specimen H shows mostly gas pores with relatively high sphericity. While the pores are mostly small, pores larger than 100 µm in diameter have also been observed (see Fig. 13).

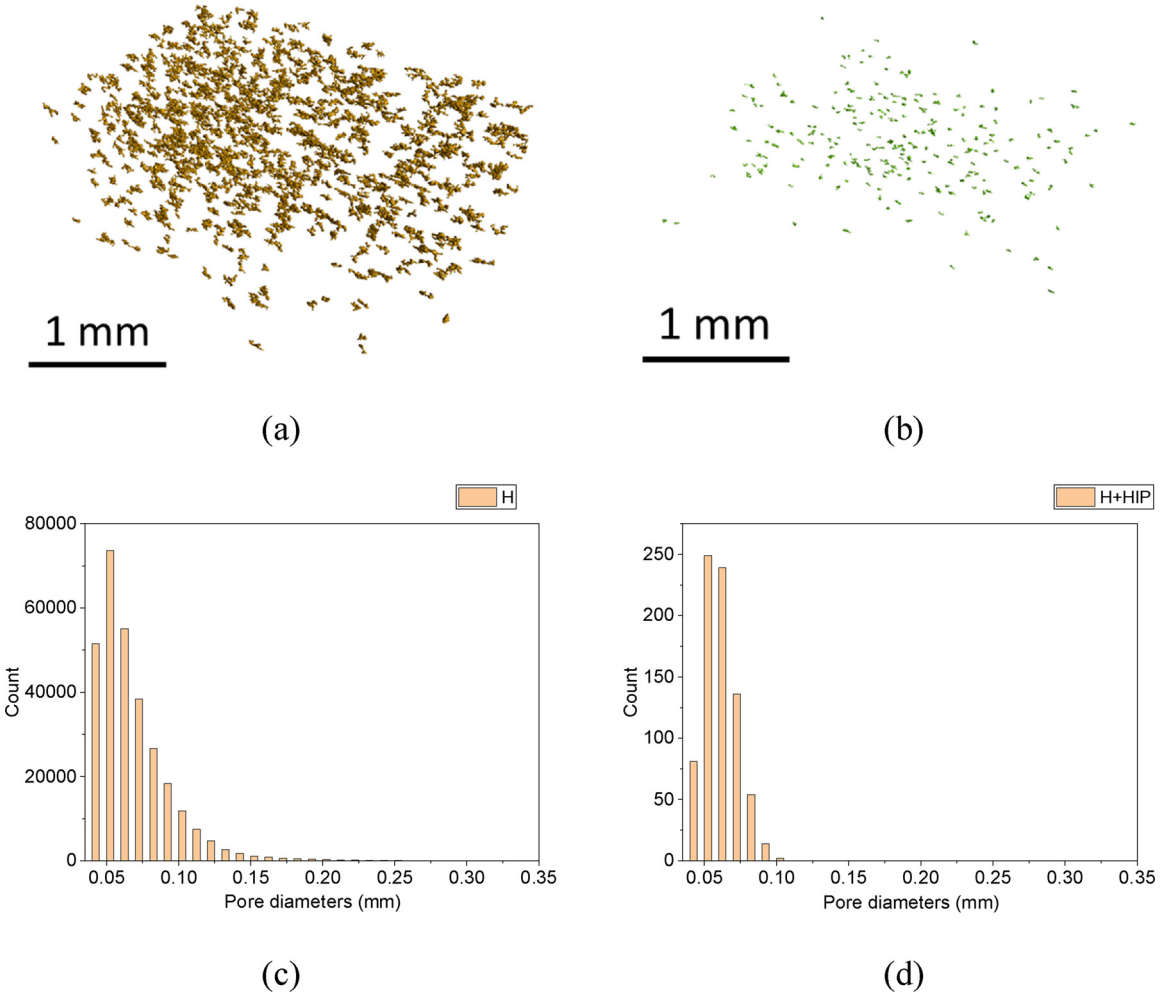

Fig. 14. Pores distribution (image and histogram) obtained from µXCT 3D scans obtained from H (a) and (c) and H + HIP (b) and (d).

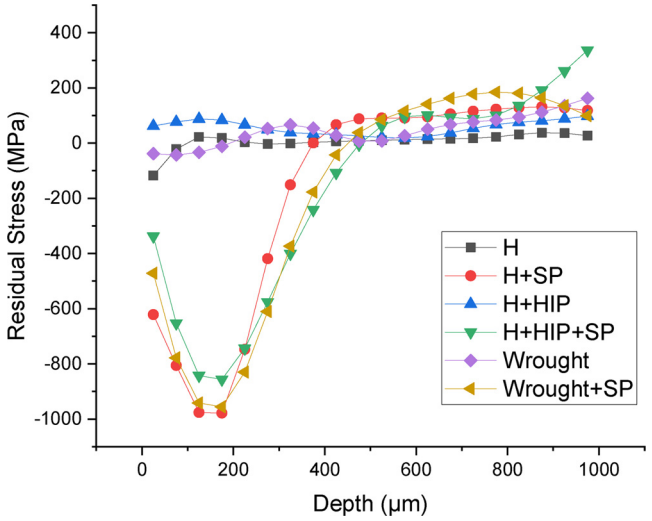

Fig. 15. Residual stress depth profiles obtained from the fatigue specimens along the loading direction.

Porosity analysis was carried out on specimens H and H + HIP to investigate the effectiveness of HIP-ing in reducing porosities in L-PBF built parts. Nearly 300 thousand pores were detected within the scanned volume of specimen H, which is significantly reduced to less than a thousand after HIP-ing. This translates to a reduction in porosity volume ratio from 0.39 % to 0.08 % after HIP-ing (refer to Fig. 14 for comparison between H and H + HIP specimens). Large pores (> 100 μm in diameter) were mostly eliminated through HIP-ing thus the pores remaining after HIP-ing are mostly in the size range of 40–100 μm). Pores were found to be scattered randomly across the specimen with no particular areas of concentration. Previous studies reported high concentration of pores at the boundary between core and shell where different scanning strategies are employed [13]. In this study however, this boundary has been removed via machining which explains for the absence of regions with elevated concentration of pores.

3.4. Surface integrity after shot peening

Thermally originated residual stresses are expected from the L-PBF process resulting in high tensile stresses in the near surface [42]. Tensile residual stresses of up to 900 MPa within 1 mm from the free surface have been reported for L-PBF IN718 [43]. These tensile stresses appear to have been largely eliminated by the solution annealing and aging heat treatment in this study (see Fig. 11). A thin layer of compressive residual stressed layer (around 80 μm) can be observed in specimen H which can be attributed to volumetric contraction mismatch resulting from the thermal gradient during cooling. The compressive stresses in the near surface were no longer present after HIP-ing (specimen H + HIP). Residual stresses in the H + HIP specimen were relatively insignificant throughout the depth of the measurement.

High compressive residual stresses were introduced in the sub-surface region after shot peening for both heat-treated (H + SP) and HIP-ed specimens (H + HIP + SP). Similar magnitudes of compressive residual stresses were obtained from shot peening of conventionally produced IN 718 (see wrought + SP in Fig. 15). The same heat treatment (solutionising followed by double aging) was applied to the wrought alloy prior to shot peening. The results suggest that shot peening parameters developed for conventionally produced can also be applied to that of L-PBF built parts. The depth of compressive stressed layer is around 400 μm owing to the relatively high intensity being used for the shot peening. The compressive stresses reach its peak at the depth of around 180 μm. Interestingly, a slight difference was observed between the stress profiles obtained from H + SP and H + HIP + SP. The specimen H + HIP + SP exhibited a lower peak compressive residual stress compared to that of specimen H + SP. This is likely to be associated with the reduction in tensile strength and hardness due to γ" solutionisation after HIP-ing as verified by the nano-indentation test results in the bulk material (refer to Fig. 16a). The depth of the compressive stressed layer in specimen H + HIP + SP was also found to be slightly higher than that of H + SP. It is also interesting to note that the residual stress profile in specimen H + HIP + SP suggests high balancing tensile residual stresses which may result in a region susceptible towards early fatigue cracking.

Kernel averaged misorientation (KAM) maps for the different specimens are shown in Fig. 17. Fairly large amount of dislocations could be seen in the bulk of specimen P (Fig. 17a) indicating presences of plastic strains developed during the L-PBF process consistent with a published study [44]. Heat treatment and HIP-ing can be seen to relieve these internal strains and dislocations (Fig. 17b–c). Significant work hardening could be observed from shot peening (Fig. 17d–e).. The depth of cold work introduced by post-processes can be estimated from the local misorientations [45–47]. Interestingly the depth of the work hardened layer of specimen H + HIP + SP is closely related to the depth of the compressive residual stressed layer unlike that in specimen H + SP. While the KAM data reveals significant changes in misorientations following peening, it does not show significant variation

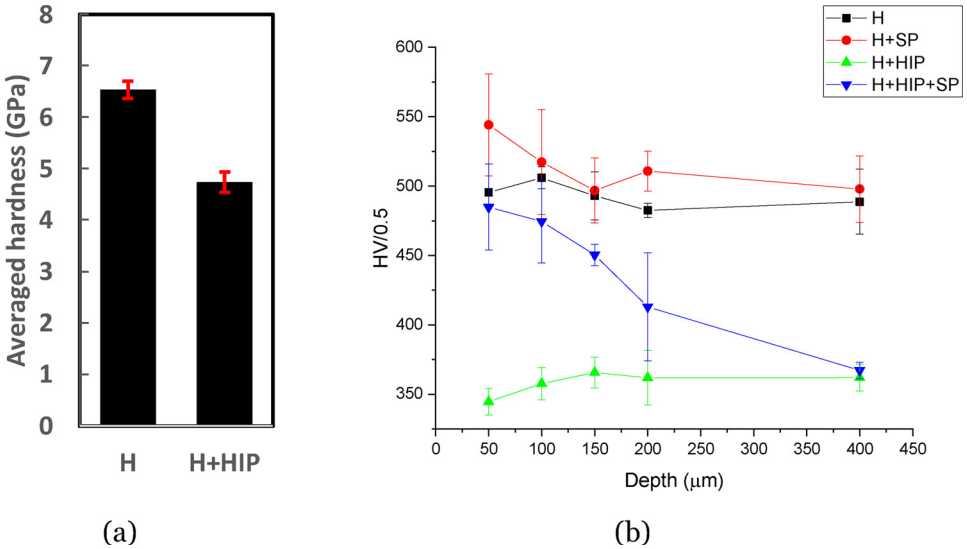

Fig. 16. Hardness data collected from nano-indentation (a) as well as micro-indentation (b) experiments. A series of micro-indentations were completed to investigate hardness variation with depth (distance from free surface) as shown in (b). Note that variation in the hardness values in the bulk obtained from nano- and micro-indentation is related to the indentation size effect.

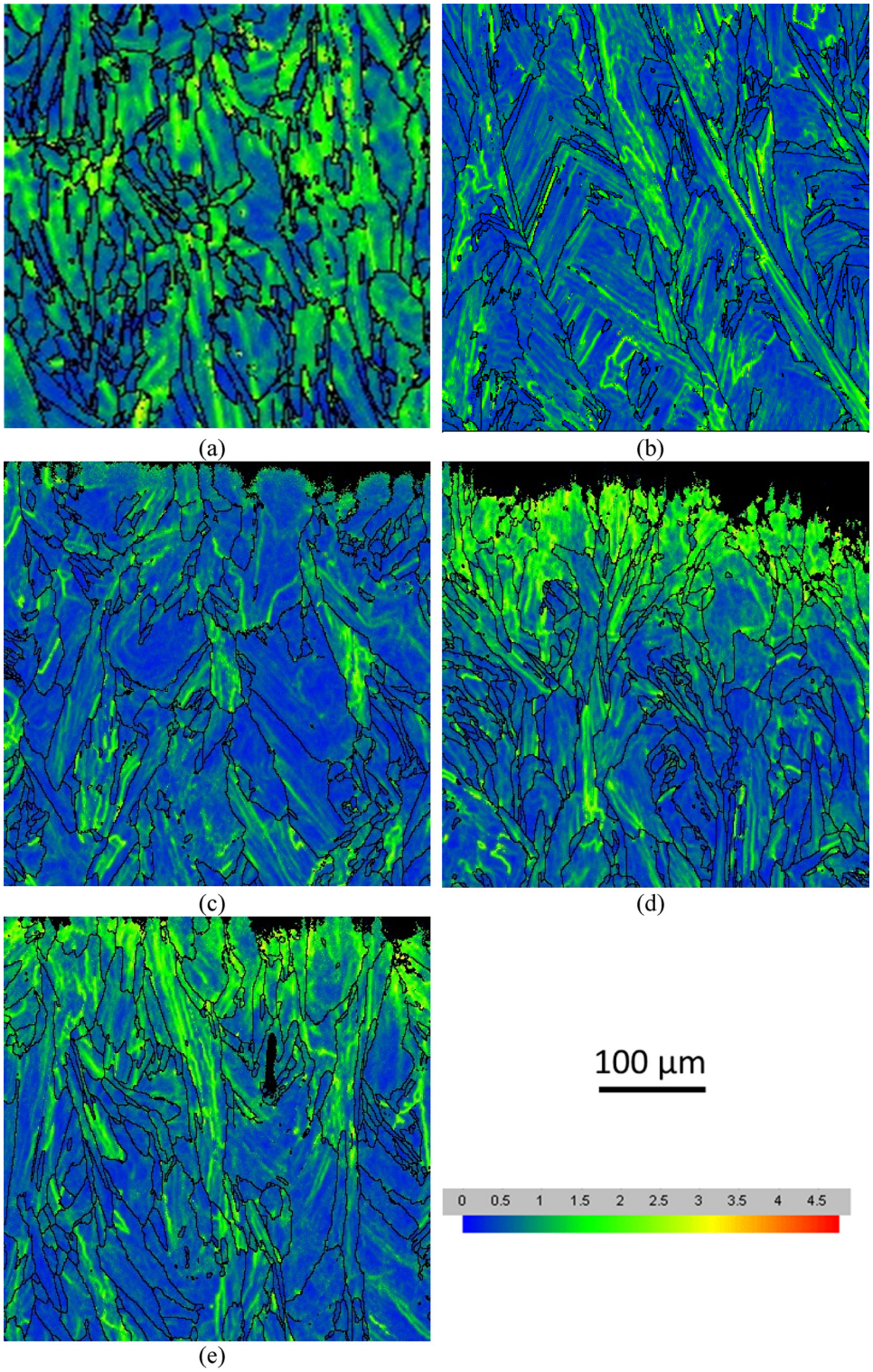

Fig. 17. Kernel Averaged Misorientation (KAM) maps of the different specimens: (a)P, (b) H, (c) H + HIP, (d) H + SP and (e) H + HIP + SP.

between H + SP and H + HIP + SP specimens to explain the variation in the extent of work hardening due to shot peening on the two specimens. The grain sizes also do not appear to have been altered significantly from shot peening. The increase in hardness following shot peening can be attributed to dislocations formation shown in the KAM maps as well as compressive residual stresses.

The amount of cold work is known to influence the stability of residual stress states under fatigue loading [48]. Increase in the amount of cold work has been associated with greater stress relaxation under mechanical [48] or thermal loads [49]. Comparing the two shot peened specimens (H + SP and H + HIP + SP), the magnitude and extent by which cold work is imparted in the material appear to be very similar from the KAM maps shown in Fig. 17. This suggests little variation in terms of residual stresses relaxation under fatigue loads between the two types of specimens.

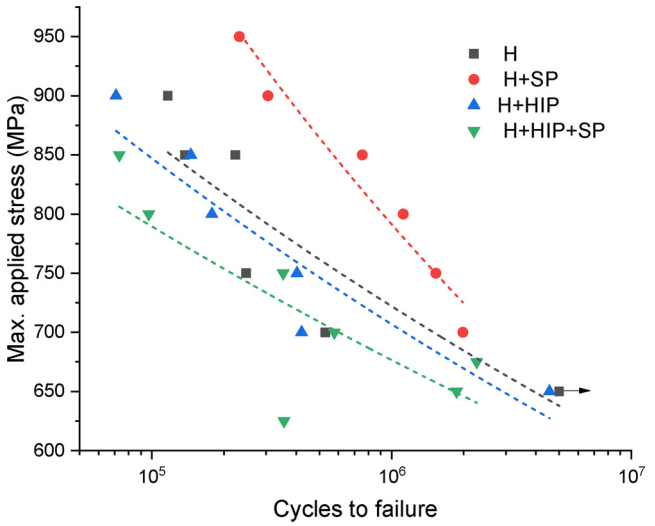

Fig. 18. Peak stress vs cycle-to-failure (S-N) plot for the different types of specimens with trend lines superimposed. Black arrow indicates run-out.

3.5. Fatigue performance evaluation

S-N plots obtained from L-PBF IN718 specimens are shown in Fig. 18. The trend lines were plotted using exponential fit (following the equation $S = A + me^N$, where S the max. applied stress, N the cycles to failure, A and m are fitting parameters) with fatigue limits at around 10^6 cycles according to ASTM E468. Specimens H + SP exhibit the best fatigue performance, showing significant improvement in fatigue lives over specimens H at all the stress levels tested. Both surface and sub-surface crack initiations were observed in H + SP specimens, even on the same fractured surface (Fig. 19a). It is interesting that the location of the sub-surface initiation varies widely among the H + SP specimens with some specimens showing sub-surface initiation site within the compressive stressed region (< 400 μm) and others well within the bulk of the specimen (Fig. 19b).

Fractography evaluations revealed crack initiations mainly in the sub-surface region for specimen H. As expected in this type of specimen, the crack initiations are associated with defects (porosities, brittle phases or inclusions) located near the free surface. A crack initiation site was observed at around 100 μm away from the free surface for a specimen H tested at 850 MPa (see Fig. 20) close to what appears to be a cluster of small pores.

HIP-ing was not found to improve the fatigue performance from condition H as shown by the close overlapping between the H and H + HIP stress-life data in Fig. 18. HIP is expected to improve fatigue performance by reducing the size or eliminating porosities and this was found to be effective as fractographs from specimens H + HIP show little evidence of pores around the fatigue fracture surface (see Fig. 21). However, HIP-ing was not effective in eliminating the brittle phases as well as inclusions which were found around the fracture surface (see Fig. 21). This coupled with the reduction in strength and resistance to plastic deformation associated with solutionisation of γ" precipitates during HIP process above the gamma solvus resulted in the absence of a net effect in terms of fatigue performance.

Shot peening of the HIP-ed specimens (H + HIP + SP) resulted in reduced fatigue performance as shown in the stress-life plot. While rough surface due to shot peening is detrimental to fatigue performance, this is not expected to be the main contributor to fatigue debit since similar level of roughness is seen in H + SP specimens. Fractography of specimens H + HIP + SP revealed initiation sites in the subsurface approximately 300 μm away from the free surface (see Fig. 22) near the transition from compressive to tensile stressed regions. This suggests interactions between balancing tensile residual stresses and sub-surface defects which are detrimental to the fatigue performance. This has also been reported in a similar study [50]. The detrimental effects from tensile stresses were dominant and therefore override the beneficial impact that the compressive stressed layer provides.

4. Conclusions

In this study, a comprehensive investigation of fatigue performance of L-PBF IN718 with different post-processing routes were carried out. Fatigue tests in load-control were carried out to study the effectiveness of HIP and shot peening in improving fatigue performance. The main findings are summarised below:

- Shot peening was found to be effective in developing compressive residual stressed layer in L-PBF specimens. Residual stress profiles obtained from L-PBF specimens were found to be comparable to that of conventionally manufactured alloy. In view of the high intensity level employed during shot peening, a compressive stressed layer of up to 400 μm was developed with the magnitude of the maximum compressive stress approaching the yield strength of the material.
- A slight reduction in compressive stresses was observed on the specimen H + HIP + SP when compared to specimen H + SP. This can be attributed to the variation in yield strength due to γ" solutionisation after HIP-ing.
- HIP-ing was found to be effective in reducing the quantity as well as size of pores within the specimens, reducing the porosity volume ratio from 0.39 % to 0.08 %. However, its effectiveness in improving fatigue performance was not realised due to the presence of inclusions and brittle phases within the materials as well as the reduction in yield strength due to HIP-ing.
- The effects of shot peening on fatigue performance were found to be strongly dependent on the microstructure as well as defects within

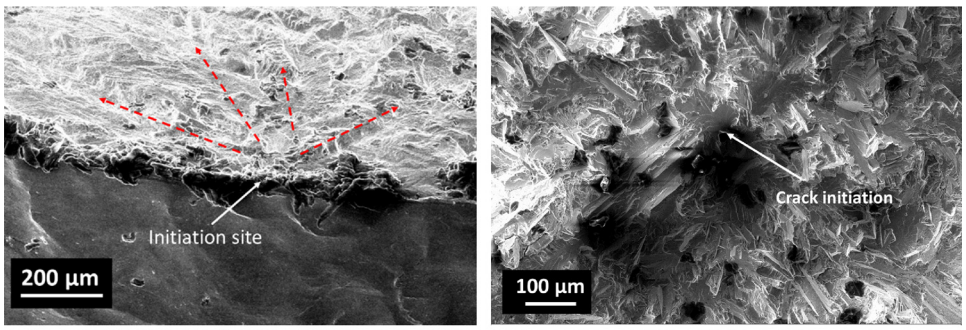

Fig. 19. Secondary electron micrographs taken from specimen H + SP tested at: (a) 900 MPa showing crack initiation at the surface and sub-surface and (b) 700 MPa showing crack initiation at the bulk material.

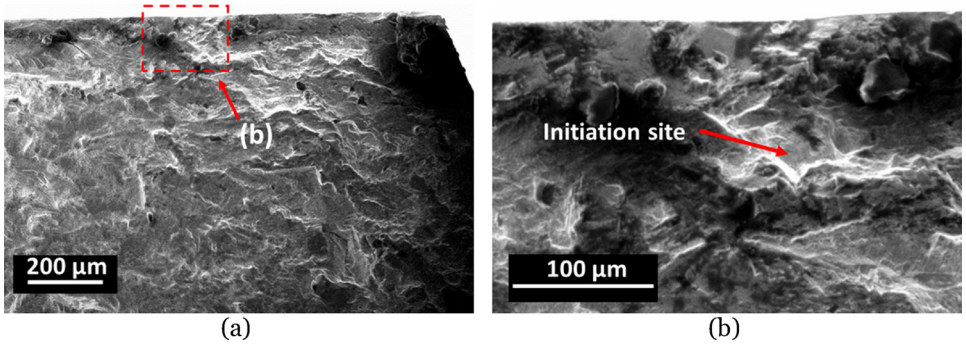

Fig. 20. Secondary electron micrographs taken from specimen H tested at 850 MPa: (a) Low magnification image and (b) high magnification image showing the crack initiation site.

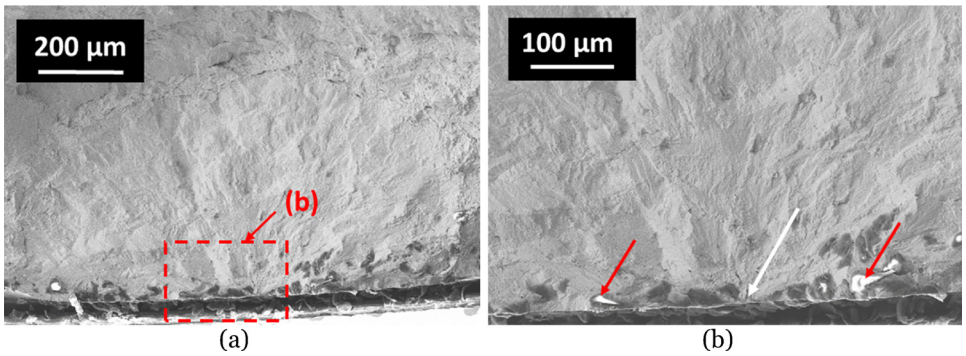

Fig. 21. Secondary electron micrographs taken from specimen H + HIP tested at 900 MPa: (a) Low magnification image and (b) high magnification image showing the crack initiation site (white arrow) as well as Nb-rich inclusions (red arrows).

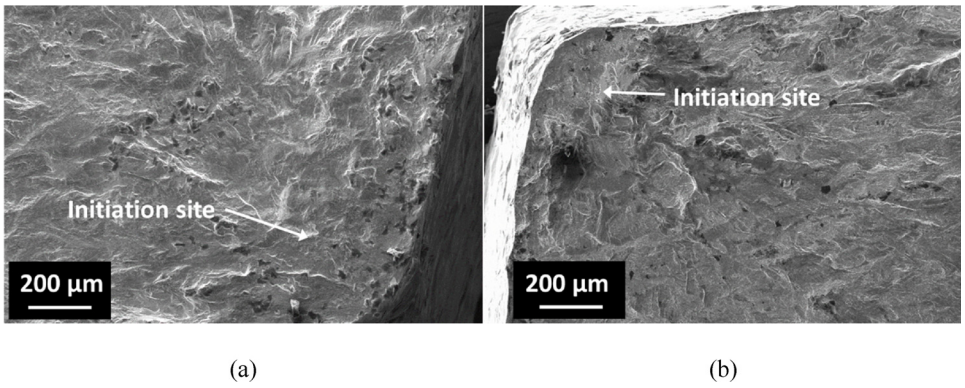

Fig. 22. Secondary electron micrographs taken from specimen H + HIP + SP tested at: (a) 800 MPa and (b) 625 MPa showing crack initiation at the sub-surface, approximately 300 µm away from the free- surface.

the alloy prior to shot peening. While improvements in fatigue performance were observed on specimens H + SP, the opposite was observed for specimens H + HIP + SP where detrimental effects from the balancing tensile stresses were dominant. This was evident from the sub-surface initiated cracks shown from the fractography of H + HIP + SP.

CRediT authorship contribution statement

Dennise Tanoko Ardi: Conceptualization, Methodology, Formal analysis, Writing - review & editing, Visualization, Project administration. **Lim Guowei:** Methodology, Investigation. **Niroj Maharjan:** Validation, Investigation, Writing - review & editing. **Bisma Mutiargo:** Methodology, Investigation. **Seng Hwee Leng:** Validation, Investigation. **Raghavan Srinivasan:** Methodology, Formal analysis, Writing - review & editing.

Declaration of Competing Interest

The authors declare that they have no known competing financial interests or personal relationships that could have appeared to influence the work reported in this paper.

Acknowledgements

The funding for this study was provided by Advanced Remanufacturing and Technology Centre (ARTC) under Core Research Project 5 (CRP5 – C18_09_ARTC). The authors thank Cheng Wei Shin and Krishnan Manickavasagam for their assistance in fatigue and L-PBF experimental trials as well as Meng Tzee Luai for the nano-indentation tests.

References

[1] S. Tammas-Williams, P.J. Withers, I. Todd, P.B. Prangnell, The influence of porosity on fatigue crack initiation in additively manufactured titanium components, Sci. Rep. 7 (1) (2017) 7308 2017/08/04.

[2] A.R. Balachandramurthi, J. Moverare, N. Dixit, R. Pederson, Influence of defects and as-built surface roughness on fatigue properties of additively manufactured Alloy 718, Mater. Sci. Eng. A 735 (2018) 463–474 2018/09/26/.

[3] L.L. Parimi, R. G. A, D. Clark, M.M. Attallah, Microstructural and texture development in direct laser fabricated IN718, Mater. Charact. 89 (2014) 102–111.

[4] H. Qi, M. Azer, A. Ritter, Studies of standard heat treatment effects on microstructure and mechanical properties of laser net shape manufactured INCONEL 718, Metall. Mater. Trans. A 40 (10) (2009) 2410–2422 2009/10/01.

[5] P. Kumar, J. Farah, J. Akram, C. Teng, J. Ginn, M. Misra, Influence of laser processing parameters on porosity in Inconel 718 during additive manufacturing, Int. J. Adv. Manuf. Technol. 103 (1) (2019) 1497–1507 2019/07/01.

[6] T. Vilaro, C. Colin, J.D. Bartout, As-fabricated and heat-treated microstructures of the Ti-6Al-4V alloy processed by selective laser melting, Metall. Mater. Trans. A 42 (10) (2011) 3190–3199 2011/10/01.

[7] H. Gong, K. Rafi, H. Gu, T. Starr, B. Stucker, Analysis of defect generation in Ti–6Al–4V parts made using powder bed fusion additive manufacturing processes, Addit. Manuf. 1-4 (2014) 87–98 2014/10/01/.

[8] J.J.S. Dilip, et al., Influence of processing parameters on the evolution of melt pool, porosity, and microstructures in Ti-6Al-4V alloy parts fabricated by selective laser melting, Prog. Addit. Manuf. 2 (3) (2017) 157–167 2017/09/01.

[9] S. Tammas-Williams, P.J. Withers, I. Todd, P.B. Prangell, The effectiveness of hot isostatic pressing for closing porosity in titanium parts manufactured by selective electron beam melting, Metall. Mater. Trans. A 47A (2016) 1939–1946.

[10] M. Balbaa, S. Mekhiel, M. Elbestawi, J. McIsaac, On selective laser melting of Inconel 718: densification, surface roughness, and residual stresses, Mater. Des. (2020) 108818 2020/05/22/.

[11] N. Nadammal, et al., Effect of hatch length on the development of microstructure, texture and residual stresses in selective laser melted superalloy Inconel 718, Mater. Des. 134 (2017) 139–150 2017/11/15/.

[12] K. Moussaoui, W. Rubio, M. Mousseigne, T. Sultan, F. Rezai, Effects of Selective Laser melting additive manufacturing parameters of Inconel 718 on porosity, microstructure and mechanical properties, Mater. Sci. Eng. A 735 (2018) 182–190 2018/09/26/.

[13] W. Tillmann, C. Schaak, J. Nellesen, M. Schaper, M.E. Aydinöz, K.-P. Hoyer, Hot isostatic pressing of IN718 components manufactured by selective laser melting, Addit. Manuf. 13 (2017) 93–102.

[14] S.-C. Lee, S.-H. Chang, T.-P. Tang, H.-H. Ho, J.-K. Chen, Improvement in the Microstructure and Tensile Properties of Inconel 718 Superalloy by HIP Treatment, Mater. Trans. 47 (11) (2006) 2877–2881.

[15] D.H. Smith, et al., Microstructure and mechanical behavior of direct metal laser sintered Inconel alloy 718, Mater. Charact. 113 (2016) 1–9 2016/03/01/.

[16] M.E. Aydinoz, F. Brenne, M. Schaper, C. Schaak, W. Tillmann, J. Nellesen, On the microstructural and mechanical properties of post-treated additively manufactured Inconel 718 superalloy under quasi-static and cyclic loading, Mater. Sci. Eng. A 669 (2016) 246–258.

[17] D.A. Lesyk, S. Martinez, B.N. Mordyuk, V.V. Dzhemelinskyi, A. Lamikiz, G.I. Prokopenko, Post-processing of the Inconel 718 alloy parts fabricated by selective laser melting: Effects of mechanical surface treatments on surface topography, porosity, hardness and residual stress, Surf. Coat. Technol. 381 (2020) 125136 2020/01/15/.

[18] W. Zhuang, Q. Liu, R. Djugum, P.K. Sharp, A. Paradowska, Deep surface rolling for fatigue life enhancement of laser clad aircraft aluminium alloy, Appl. Surf. Sci. 320 (2014) 558–562.

[19] B. AlMangour, J.-M. Yang, Improving the surface quality and mechanical properties by shot peening of 17-4 stainless steel fabricated by additive manufacturing, Mater. Des. 110 (2016) 914–924.

[20] N.E. Uzan, S. Ramati, R. Shneck, N. Frage, O. Yeheskel, On the effect of shot-peening on fatigue resistance of AlSi10Mg specimens fabricated by additive manufacturing using selective laser melting (AM-SLM), Addit. Manuf. 21 (2018) 458–464 2018/05/01/.

[21] L. Hackel, J. R.Rankin, A. Rubenchik, W. E.King, M. Matthews, Laser peening: a tool for additive manufacturing post-processing, Addit. Manuf. 24 (2018) 67–75.

[22] S. Luo, W. He, K. Chen, X. Nie, L. Zhou, Y. Li, Regain the fatigue strength of laser additive manufactured Ti alloy via laser shock peening, J. Alloys. Compd. 750 (2018) 626–635 2018/06/25/.

[23] N. Kalentics, M.O.V. de Seijas, S. Griffiths, C. Leinenbach, R.E. Logé, 3D laser shock peening – a new method for improving fatigue properties of selective laser melted parts, Addit. Manuf. 33 (2020) 101112 2020/05/01/.

[24] N. Kalentics, et al., 3D laser shock peening – a new method for the 3D control of residual stresses in Selective Laser Melting, Mater. Des. 130 (2017) 350–356 2017/09/15/.

[25] J. Gu, J. Ding, S.W. Williams, H. Gu, P. Ma, Y. Zhai, The effect of inter-layer cold working and post-deposition heat treatment on porosity in additively manufactured aluminum alloys, J. Mater. Process. Technol. 230 (2016) 26–34 2016/04/01/.

[26] B. Farber, et al., Correlation of mechanical properties to microstructure in Inconel 718 fabricated by Direct Metal Laser Sintering, Mater. Sci. Eng. A 712 (2018) 539–547 2018/01/17/.

[27] E. Hosseini, V.A. Popovich, A review of mechanical properties of additively manufactured Inconel 718, Addit. Manuf. 30 (2019) 100877 2019/12/01/.

[28] R. Konečná, G. Nicoletto, L. Kunz, A. Bača, Microstructure and directional fatigue behavior of Inconel 718 produced by selective laser melting, Procedia Struct. Integr. 2 (2016) 2381–2388 2016/01/01/.

[29] S. Gribbin, J. Bicknell, L. Jorgensen, I. Tsukrov, M. Knezevic, Low cycle fatigue behaviour of direct metal laser sintered Inconel alloy 718, Int. J. Fatigue 93 (2016) 156–167.

[30] A.R. Balachandramurthi, J. Moverare, N. Dixit, D. Deng, R. Pederson, Microstructural influence on fatigue crack propagation during high cycle fatigue testing of additively manufactured Alloy 718, Mater. Charact. 149 (2019) 82–94 2019/03/01/.

[31] C. Aumund-Kopp, F. Petzoldt, Laser sintering of parts with complex internal structures, PM World Congress (2008).

[32] D. Manfredi, F. Calignano, M. Krishnan, R. Canali, E.P. Ambrosio, E. Atzeni, From powders to dense metal parts: characterization of a commercial AlSiMg alloy processed through direct metal laser sintering, MDPI Mater. 6 (2013) 856–869.

[33] F. Liu, X. Lin, G. Yang, M. Song, J. Chen, W. Huang, Recrystallization and its influence on microstructures and mechanical properties of laser solid formed nickel base superalloy Inconel 718, Rare Met. 30 (2011) 433–438.

[34] M. Cloots, K. Kunze, P.J. Uggowitzer, K. Wegener, Microstructural characteristics of the nickel-based alloy IN738LC and the cobalt-based alloy Mar-M509 produced by selective laser melting, Mater. Sci. Eng. A 658 (2016) 68–76.

[35] V.D. Divya, et al., Microstructure of selective laser melted CM247LC nickel-based superalloy and its evolution through heat treatment, Mater. Charact. 114 (2016) 62–74.

[36] S. Sui, J. Chen, E. Fan, H. Yang, X. Lin, W. Huang, The influence of Laves phases on the high-cycle fatigue behavior of laser additive manufactured Inconel 718, Mater. Sci. Eng. A 695 (2017) 6–13 2017/05/17/.

[37] S. Azadian, L.-Y. Wei, R. Warren, Delta phase precipitation in Inconel 718, Mater. Charact. 53 (1) (2004) 7–16 2004/09/01/.

[38] S. Suia, J. Chena, E. Fana, H. Yanga, X. Lina, W. Huang, The influence of Laves phases on the high-cycle fatigue behavior of laser additive manufactured Inconel 718, Mater. Sci. Eng. A 695 (2017) 6–13.

[39] A. Mostafa, I.P. Rubio, V. Brailovski, M. Jahazi, M. Medraj, Structure, texture and phases in 3D printed IN718 alloy subjected to homogenization and HIP treatments, MDPI Met. 7 (6) (2017).

[40] K.N. Amato, et al., Microstructures and mechanical behavior of Inconel 718 fabricated by selective laser melting, Acta Mater. 60 (5) (2012) 2229–2239.

[41] D. Zhang, W. Niu, X. Cao, Z. Liu, Effect of standard heat treatment on the microstructure and mechanical properties of selective laser melting manufactured Inconel 718 superalloy, Mater. Sci. Eng. A 644 (17) (2015) 32–40.

[42] B. Ahmad, S.O. van der Veen, M.E. Fitzpatrick, H. Guo, Residual stress evaluation in selective-laser-melting additively manufactured titanium (Ti-6Al-4V) and inconel 718 using the contour method and numerical simulation, Addit. Manuf. 22 (2018) 571–582 2018/08/01/.

[43] R. Barros, et al., Laser powder bed fusion of Inconel 718: residual stress analysis before and after heat treatment, Metals 9 (12) (2019).

[44] D. Deng, R.L. Peng, H. Brodin, J. Moverare, Microstructure and mechanical properties of Inconel 718 produced by selective laser melting: sample orientation dependence and effects of post heat treatments, Mater. Sci. Eng. A 713 (2018) 294–306 2018/01/24/.

[45] B.J. Foss, S. Gray, M.C. Hardy, S. Stekovic, D.S. McPhail, B.A. Shollock, Analysis of shot-peening and residual stress relaxation in the nickel-based superalloy RR1000, Acta Mater. (2013).

[46] K.A. Soady, B.G. Mellor, G.D. West, G. Harrison, A. Morris, P.A.S. Reed, Evaluating surface deformation and near surface strain hardening resulting from shot peening a tempered martensitic steel and application to low cycle fatigue, Int. J. Fatigue 54 (2013) 106–117.

[47] D.J. Child, G.D. West, R.C. Thomson, Assessment of surface hardening effects from shot peening on a Ni-based alloy using electron backscatter diffraction techniques, Acta Mater. 59 (12) (2011) 4825–4834 2011/07/01/.

[48] L. Angkurarach, P. Juijerm, Effects of high-temperature deep rolling on fatigue, work hardening, and residual stress relaxation of martensitic stainless steel AISI 420, J. Mater. Eng. Perform. 29 (2) (2020) 1416–1423 2020/02/01.

[49] P. Prevey, D. Hombach, P. Mason, Thermal Residual Stress Relaxation and Distortion in Surface Enhanced Gas Turbine Engine Components, Defense Technical Information Centre, 1998.

[50] E. Salvati, A.J.G. Lunt, C.P. Heason, G.J. Baxter, A.M. Korsunsky, An analysis of fatigue failure mechanisms in an additively manufactured and shot peened IN 718 nickel superalloy, Mater. Des. 191 (2020) 108605 2020/06/01/.